Ultrafast Transitions from Solid to Liquid and Plasma States of Graphite Induced by X-Ray Free-Electron Laser Pulses

S. P. Hau-Riege,[1,*] A. Graf,[1] T. Döppner,[1] R. A. London,[1] J. Krzywinski,[2] C. Fortmann,[1] S. H. Glenzer,[1] M. Frank,[1] K. Sokolowski-Tinten,[3] M. Messerschmidt,[2] C. Bostedt,[2] S. Schorb,[2] J. A. Bradley,[1] A. Lutman,[2] D. Rolles,[4,5] A. Rudenko,[4,6] and B. Rudek[4,6]

[1]*Lawrence Livermore National Laboratory, Livermore, California 94550, USA*
[2]*SLAC National Accelerator Laboratory, Menlo Park, California 94025, USA*
[3]*Faculty of Physics and Center for Nanointegration Duisburg-Essen (CENIDE), University of Duisburg-Essen 47048, Duisburg, Germany*
[4]*Max Planck Advanced Study Group, Center for Free Electron Laser Science, 22761 Hamburg, Germany*
[5]*Max Planck Institut für Medizinische Forschung, 69120 Heidelberg, Germany*
[6]*Max Planck Institut für Kernphysik, 69117 Heidelberg, Germany*

(Received 3 November 2011; published 23 May 2012)

We used photon pulses from an x-ray free-electron laser to study ultrafast x-ray-induced transitions of graphite from solid to liquid and plasma states. This was accomplished by isochoric heating of graphite samples and simultaneous probing via Bragg and diffuse scattering at high time resolution. We observe that disintegration of the crystal lattice and ion heating of up to 5 eV occur within tens of femtoseconds. The threshold fluence for Bragg-peak degradation is smaller and the ion-heating rate is faster than current x-ray-matter interaction models predict.

DOI: 10.1103/PhysRevLett.108.217402 PACS numbers: 78.47.J−, 52.70.La, 78.40.Ri, 78.70.Dm

Ultrafast phase transitions from solid to liquid and plasma states are important in the development of novel material-synthesis techniques [1], in ultrafast imaging [2,3], and in high-energy-density science [4]. Triggered by intense photon pulses in the laboratory, such phase transitions are complex. The kinetics of *optical* photon-induced transitions has been studied extensively [1,5,6]. Optical photons are absorbed through collective electronic processes [7]. In contrast, x-ray-induced dynamics are expected to differ substantially because x rays generate high-energy photoelectrons that equilibrate through collisional ionization and develop into a hot electron gas. Additionally, x rays penetrate materials to depths of more than 1 μm, whereas optical penetration depths are rather short (~ 10 nm). The emergence of x-ray free-electron lasers (XFELs) now enables the study of ultrafast x-ray-induced transitions at extremely high time resolution and over a large, isochorically heated volume.

We used pulses from an XFEL to excite graphite isochorically to extreme conditions with electron temperatures up to about 10 eV [8]. This induced ultrafast electronic processes and, ultimately, an order-disorder transformation. We characterized the x-ray-induced ultrafast ionization, lattice destruction, and temperature-relaxation dynamics with a temporal resolution of tens of femtoseconds by measuring the dynamic structure factor, $S(k, \omega)$, simultaneously both on and off the Bragg resonance. At low x-ray intensities, the crystal structure stays intact, the Bragg peak is very strong, and diffuse scattering is weak. With increasing intensities, the Bragg peak degrades due to atomic ionization and motion, and the forward diffuse elastic-scattering signal increases correspondingly. The combined measurements of the pulse-width dependence and fluence dependence of these signals allowed us to extract the ion temperature as a function of time.

We performed the experiments at the Linac Coherent Light Source (LCLS) [9], using an x-ray energy of 2 keV, pulse energies of up to 2.8 mJ, and pulse durations of 40, 60, and 80 fs. We determined the multiple-shot averaged x-ray pulse duration from statistical analysis of single-shot spectra within an error of 30% [10]. The pulse energy was measured for each shot using an upstream nitrogen-fluorescence detector [11]. The transmission of the beam line was about $(15 \pm 3)\%$ [12]. The focal spot area was determined from microscopic analysis of low-fluence beam imprints in yttrium aluminum garnet [13]. We focused the x-ray pulses to a beam area of 36–10 μm^2 onto a highly oriented pyrolytic-graphite (HOPG) crystal, as illustrated in Fig. 1. With this transmission and beam area, we obtained intensities up to 2.9×10^{16} W/cm^2. The crystal was mounted on an x-y-z movable rotation stage, which was moved 250 μm or more between shots. The x-ray fluence was varied from 0.02 to 1.2 kJ/cm^2 with a gas attenuator. HOPG comprises a mosaic structure of highly oriented graphite crystallites, with an out-of-plane angular spread of approximately 0.4° FWHM or less. In the following we report our results as a function of *peak* fluences and intensities at the center of the roughly Gaussian beam.

We recorded the Bragg and diffuse scattering signals from the same pulse that heats the target. Using an x-ray

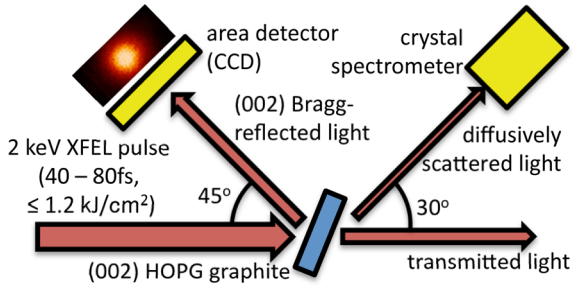

FIG. 1 (color online). Experimental setup to characterize the response of the graphite crystal simultaneously through elastic and inelastic diffuse scattering and Bragg scattering.

area detector (CCD) protected by a diamond foil attenuator, we observed the back-reflected (002) Bragg peak, which is sensitive to disturbances perpendicular to the graphene layers of the 1-mm-thick HOPG crystal. The Bragg angle for this configuration is $\sin^{-1}(\lambda/2d) = 67.9°$, where $\lambda = 6.20$ Å is the x-ray wavelength and $d = 3.35$ Å is the graphene spacing. We also measured the single-pulse off-Bragg (diffuse) forward scattering spectrum from thin HOPG films (15 μm) with a scattering angle of 30° (scattering vector $k \approx 0.52$ Å^{-1}) using a curved HOPG crystal spectrometer (close to von Hamos geometry [14]) with a resolution of 3.5 eV and a spectral width of 300 eV. Off resonance (''diffuse'' or ''Thomson'') x-ray scattering [15] has been developed and applied recently to study high-energy density plasmas using longer-wavelength XFELs [16].

A typical measured Bragg spot is shown in Fig. 1 and the spot intensities versus the peak x-ray fluence for 40 and 80-fs-long pulses are shown in Fig. 2. The intensities were evaluated by fitting two-dimensional Gaussians to the Bragg spot image. Each data point in Fig. 2 represents an average of 5–10 individual shots. For 40 fs pulses, we see a prominent drop in the reflectivity (by a factor of 2.5) between 0.018 and 0.03 kJ/cm^2 and a total drop by a factor of 8 above 0.5 kJ/cm^2. For 80 fs pulses, we see a drop by a factor of 3.3 between the lowest available fluence (0.022 kJ/cm^2) and fluences above 0.5 kJ/cm^2. The initial drop at low fluences is not seen for 80 fs pulses, possibly due to the lack of very low-fluence data.

It is expected that two effects contribute to the degradation of the Bragg intensity: atomic motion and ionization. The effect of atomic motion can be estimated from the Debye-Waller factor $D = \exp(-2M)$ with $M = \bar{u}_s^2 k_B^2/2$, where $\bar{u}_s^2$ is the mean-square displacement of an atom from its mean position in the direction of the scattering vector k_B (i.e. perpendicular to the graphene layers). Motions of order 0.5–1 Å are needed to explain the observed intensity drops. Ionization leads to a relative intensity of $(F/F_0)^2$, where F_0 and F are the atomic scattering factors of the cold and ionized material, respectively. Assuming that F is proportional to the number of bound electrons, an ionization of about 3.6 is required to explain the observed intensity drops. Two theoretical modeling approaches were explored to calculate the Bragg degradation due to these effects. For high fluences, we considered a classical molecular dynamics (MD) model for electron and ion motion [17], including x-ray ionization and heating. This model reproduces the drop in reflectivity for the 80 fs pulses with about 20% and 80% contributions from atomic motion and ionization, respectively. However, the model underestimates the reflectivity drop for the 40 fs pulses by a factor of 2. It appears that ionization and/or motion is happening faster than the model suggests. For low fluences, the electrons are nearly degenerate and we explored a tight-binding molecular dynamics (TBMD) [18] model for this regime. With TBMD, we do not see the steep drop in reflectivity at low fluences seen in experiment for 40 fs and 80 fs pulse lengths. It is conceivable that the mild heating (by a few eV/atom) in the low-fluence regime could lead to atomic excitation and an associated drop in the atomic form factor, not included in the model, or that the applicability of the TBMD model, originally developed for the optical regime, is not correct for x rays due to the different coupling with the material and the associated electron-induced ionization cascades.

Figure 3 shows representative average diffuse scattering spectra for different pulse lengths, from which we can identify the elastic-scattering (Rayleigh) peak around

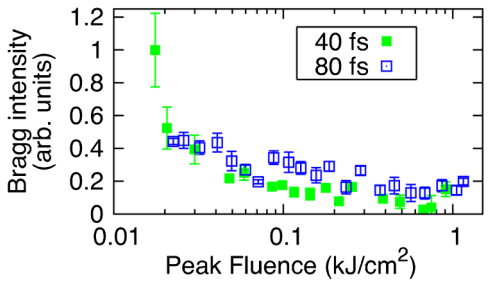

FIG. 2 (color online). Measured pulse-averaged Bragg intensity with 1σ error bars as a function of the peak fluence for two different pulse lengths.

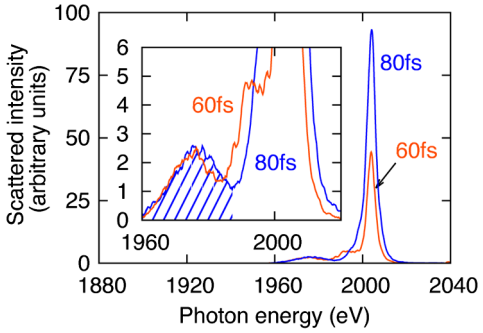

FIG. 3 (color online). Scattering spectra for 60 and 80 fs pulses.

2005 eV and the inelastic feature centered around 1970 eV. The most striking result is the pronounced increase in Rayleigh scatter with pulse length while the integral of the inelastic scattering feature remains fairly constant. Since Doppler-broadening due to ion motion is very small compared to the spectrometer resolution, the measured Rayleigh shape corresponds to the XFEL source spectrum. As ionization proceeds, we expect scattering from plasmon waves to appear at energy shifts of 10–15 eV from the Rayleigh peak. The downshifted plasmon cannot be uniquely identified due to spectral overlap with the Rayleigh feature and Compton scattering from bound electrons or L-shell Compton scattering. The absence of an upshifted plasmon feature allows us to set an upper limit on the electron temperature of 10 eV using the principle of detailed balance. The inelastic feature (shaded in Fig. 3) consists of scattering from delocalized and valence electrons [19], and its spectrally integrated signal is expected to be roughly constant as follows from Bethe f-sum rule normalization [20]. We use this property to absolutely calibrate the measured spectra. We have analyzed 20 to 50 spectra for each pulse length of 40, 60, and 80 fs. Figure 4(a) shows the integrated Rayleigh intensity (normalized to the incoming pulse energy) as a function of peak pulse intensity for different pulse lengths. For a given pulse length, this Rayleigh strength depends roughly linearly on the pulse intensities at 40 and 80 fs. For 60 fs pulse length, we only have high-intensity data. From this data set we obtained the Rayleigh strength as a function of pulse length at a fixed incident intensity, chosen to be 1.6×10^{16} W/cm^2. By identifying the contributions from different parts of the pulses we obtain the Rayleigh intensity at different time intervals, shown in Fig. 4(b). Here we assume that each XFEL pulse is constant in time (flat-top pulse), which is consistent with simulations for LCLS [9]. This Rayleigh intensity increases with time because the diffuse scattering component generally increases with decreasing Bragg intensity and increasing ion temperature.

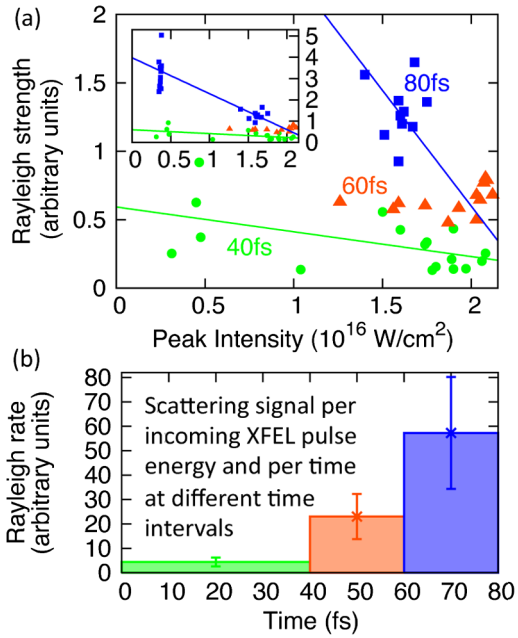

FIG. 4 (color online). (a) Integrated elastic diffuse scattering signal per incoming XFEL pulse energy for different pulse lengths and peak intensities, and a linear fit to the data. The inset shows the full data set. (b) Integrated elastic diffuse scattering signal for an intensity of 1.6×10^{16} W/cm^2.

We now analyze the diffuse scattering data (Fig. 4) to obtain information on the ionization state and ion temperature achieved in the x-ray heated plasmas. The early time (0–40 fs) diffuse Rayleigh intensity in Figs. 4(a) and 4(b) is understood to be low due to destructive interference caused by the regular crystal structure, complementary to enhanced Bragg scattering due to constructive interference. Beyond 40 fs, Bragg scattering weakens and Rayleigh scattering increases. We analyze the Rayleigh intensity using plasma-based models [21–23]. The dynamic structure factor $S(k, \omega)$ can be decomposed into terms describing near elastic scattering, (S_{Rayl}), inelastic scattering from free electrons (S_{ff}), and from bound electrons (S_b):

$$S(k, \omega) = S_{\mathrm{Rayl}}(k, \omega) + S_{\mathrm{ff}}(k, \omega) + S_b(k, \omega). \quad (1)$$

The elastic term can be written as

$$S_{\mathrm{Rayl}}(k, \omega) = |f_I(k) + q(k)|^2 S_{\mathrm{ii}}(k, \omega), \quad (2)$$

where $f_I(k)$ is the atomic form factor, $q(k)$ describes the plasma screening, and $S_{\mathrm{ii}}(k, \omega)$ is the ion-ion structure factor. Here we concentrate on the spectrally integrated quantities $S_{\mathrm{Rayl}}(k)$ and $S_{\mathrm{ii}}(k)$. Utilizing Debye-Hückel theory, the ion-ion structure factor can be written as [24]

$$S_{\mathrm{ii}}(k) = \frac{k^2 + \kappa_e^2}{k^2 + \kappa_e^2 + \kappa_i^2}, \quad (3)$$

where κ_e and κ_i are the inverse Debye length of the electrons and ions, respectively. Under the experimental conditions investigated here one can take the limit $k \to 0$ and $Z_f T_e \gg T_i$, and show that $S_{\mathrm{ii}}(k, \omega)$ scales as $T_i/Z_f T_e$:

$$S_{\mathrm{ii}}(k) \xrightarrow{k \to 0} \frac{\kappa_e^2}{\kappa_e^2 + \kappa_i^2} = \frac{1}{1 + Z_f \frac{T_e}{T_i}} \xrightarrow{Z_f T_e \gg T_i} \frac{T_i}{Z_f T_e}, \quad (4)$$

where Z_f is the ionization state, and T_i and T_e are the ion and electron temperatures, respectively. Furthermore, for the experimental parameters studied here, $|f_I(k) + q(k)|^2 \approx 24$, nearly independent of temperature. Hence within the Debye-Hückel model the integrated strength of the Rayleigh feature in the collective regime scales as

$$S_{\mathrm{Rayl}}(k) = |f_I(k) + q(k)|^2 S_{\mathrm{ii}}(k) \propto \frac{T_i}{Z_f T_e}. \quad (5)$$

Calculations of $S_{\mathrm{Rayl}}(k)$ with more sophisticated models for the ion-ion structure factor [22,25] support the

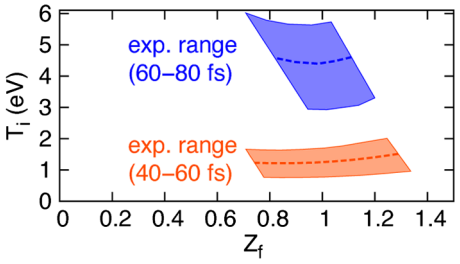

FIG. 5 (color online). Ion temperature for different times. The left (low Z_f) boundary is due to the constraint $T_e \leq 10$ eV, and the right boundary is due to $T_i \leq T_e$. The upper and lower boundaries are based on error in the Rayleigh strength in Fig. 4(a).

ion-temperature scaling derived within the Debye-Hückel model.

We then obtain two relationships for the plasma parameters T_e, T_i, and Z_f. The first is from Eq. (5). The second relation is obtained by equating the deposited x-ray energy in the graphite to the sum of the kinetic energies of the ions and electrons, and the binding energy [26]. With a maximum dose of 41 eV/atom, using the cold x-ray absorption cross section is sufficient for this estimate. Equating the measured Rayleigh strength in Fig. 4(b) to values calculated from Eq. (5), we find an allowed range of T_i and Z_f for two time intervals, as shown in Fig. 5. For the results presented in Fig. 5 we used the one-component plasma with negative screening model [22]. The results are very robust with the choice of model for calculating the ion-ion structure factor. Classical MD calculations are fairly consistent with the values constructed from the data at 50 fs, but they underestimate the ion temperature later in the pulse. Accordingly, the calculated ion-heating rate between 50 and 70 fs of 0.04 eV/fs is significantly lower than the measured rate of 0.17 eV/fs. The measured range of the charge state is 0.8 to 1.2, which agrees well with the simulation results of 0.8 to 1.0. The electron temperature in the measured data in Fig. 5, calculated using Eq. (5), ranges between T_i and 10 eV.

In summary, we pioneered a new ultrafast technique using XFEL pulses to simultaneously heat and probe materials by Bragg and diffuse x-ray scattering. We used this technique to study ultrafast order-disorder transformations in graphite providing critical information that changes our understanding of high-intensity x-ray interaction with matter. We found that the Bragg reflectivity drops at surprisingly low fluences even for relatively short ($\approx$ 40 fs) x-ray pulses, suggesting that unlike in the optical case, the reflectivity drop is associated not only with atomic motion but also significantly with an electronic process. We further found that the electron-ion coupling occurs faster than expected, which could be an obstacle for atomic-resolution single-particle imaging [2] and nanocrystallography [3] at XFELs since x-ray damage proceeds faster than anticipated.

This work was performed under the auspices of the U. S. Department of Energy (USDOE) by Lawrence Livermore National Laboratory under Contract No. DE-AC52-07NA27344. This work was funded by the Laboratory Directed Research and Development Program at LLNL. Portions of this research were carried out at the LCLS, a national user facility operated by Stanford University on behalf of the USDOE, Office of Basic Energy Sciences. K. S. T. acknowledges support by the German Research Council through the Collaborative Research Centre 616 "Energy Dissipation at Surfaces." C. F. was supported by the Alexander von Humboldt Foundation. We acknowledge support from the Max Planck Society for funding the development and operation of the CAMP instrument within the ASG at CFEL. We acknowledge support from M. Seibert during the experiments.

*Corresponding author.

[1] S. K. Sundaram and E. Mazur, Nature Mater. **1**, 217 (2002).
[2] R. Neutze, R. Wouts, D. van der Spoel, E. Weckert and J. Hajdu, Nature (London) **406**, 752 (2000).
[3] H. N. Chapman *et al.*, Nature (London) **470**, 73 (2011).
[4] R. P. Drake, *High Energy Density Physics* (Springer, New York, 2006).
[5] C. Rose-Petruck, R. Jimenez, T. Guo, A. Cavalleri, C. W. Siders, F. Rksi, J. A. Squier, B. C. Walker, K. R. Wilson, and C. P. J. Barty, Nature (London) **398**, 310 (1999).
[6] M. Eichberger, H. Schäfer, M. Krumova, M. Beyer, J. Demsar, H. Berger, G. Moriena, G. Sciaini, and R. J. D. Miller, Nature (London) **468**, 799 (2010).
[7] T. Kampfrath, L. Perfetti, F. Schapper, C. Frischkorn, and M. Wolf, Phys. Rev. Lett. **95**, 187403 (2005).
[8] See Supplemental Material at http://link.aps.org/supplemental/10.1103/PhysRevLett.108.217402 for more details about the experimental setup.
[9] LCLS Conceptual Design Report No. SLAC-R-593, 2002.
[10] A. A. Lutman, Y. Ding, Y. Feng, Z. Huang, M. Messerschmidt, J. Wu, and J. Krzywinski, Phys. Rev. ST Accel. Beams **15**, 030705 (2012).
[11] S. P. Hau-Riege *et al.*, Phys. Rev. Lett. **105**, 043003 (2010).
[12] A. A. Sorokin *et al.*, "Report on Pulse Energy Monitoring of X-Ray FEL Beam by Gas-Monitor Detector" (unpublished).
[13] J. Chalupsky *et al.*, Opt. Express **18**, 27836 (2010).
[14] L. von Hamos, Ann. Phys. (Leipzig) **409**, 716 (1933).
[15] S. H. Glenzer and R. Redmer, Rev. Mod. Phys. **81**, 1625 (2009).
[16] R. R. Fäustlin *et al.*, Phys. Rev. Lett. **104**, 125002 (2010).
[17] F. R. Graziani *et al.*, High Energy Density Phys. 8 (**2012**) 105.

[18] W. A. Harrison, *Solid State Theory* (McGraw-Hill, New York 1970).
[19] W. Schülke, U. Bonse, H. Nagasawa, A. Kaprolat, and A. Berthold, Phys. Rev. B **38**, 2112 (1988).
[20] M. Inokuti, Rev. Mod. Phys. **43**, 297 (1971).
[21] J. Chihara, J. Phys. Condens. Matter **12**, 231 (2000).
[22] D. O. Gericke, J. Vorberger, K. Wünsch, and G. Gregori, Phys. Rev. E **81**, 065401 (2010).
[23] C. Fortmann *et al.*, Laser Part. Beams **27**, 311 (2009).
[24] D. Kremp, M. Schlanges, and W.-D. Kraeft, *Quantum Statistics of Nonideal Plasmas* (Springer, New York, 2005).
[25] G. Gregori, A. Ravasio, A. Höll, S. H. Glenzer, and S. J. Rose, High Energy Density Phys. **3**, 99 (2007).
[26] M. A. Lennon *et al.*, J. Phys. Chem. Ref. Data **17**, 1285 (1988) [http://link.aip.org/link/doi/10.1063/1.555809].